JACS
JOURNAL OF THE AMERICAN CHEMICAL SOCIETY
Article
Cite This: J. Am. Chem. Soc. 2019, 141, 19655−19668
pubs.acs.org/JACS

Understanding Structure−Property Relationships of MoO_3-Promoted Rh Catalysts for Syngas Conversion to Alcohols

Arun S. Asundi,[†] Adam S. Hoffman,[‡] Pallavi Bothra,[†,§] Alexey Boubnov,[‡,▽] Fernando D. Vila,[#] Nuoya Yang,[∥] Joseph A. Singh,[⊥] Li Zeng,[†] James A. Raiford,[†] Frank Abild-Pedersen,[†,§] Simon R. Bare,[‡] and Stacey F. Bent*[,†]

[†]Department of Chemical Engineering, Stanford University, Stanford, California 94305, United States
[‡]SSRL, SLAC National Accelerator Laboratory, Menlo Park, California 94205, United States
[§]SUNCAT Center for Interface Science and Catalysis, SLAC National Accelerator Laboratory, Menlo Park, California 94205, United States
[∥]Department of Materials Science and Engineering, Stanford University, Stanford, California 94305, United States
[⊥]Department of Chemistry, Stanford University, Stanford, California 94305, United States
[#]Department of Physics, University of Washington, Seattle, Washington 98195, United States

Supporting Information

ABSTRACT: Rh-based catalysts have shown promise for the direct conversion of syngas to higher oxygenates. Although improvements in higher oxygenate yield have been achieved by combining Rh with metal oxide promoters, details of the structure of the promoted catalyst and the role of the promoter in enhancing catalytic performance are not well understood. In this work, we show that MoO_3-promoted Rh nanoparticles form a novel catalyst structure in which Mo substitutes into the Rh surface, leading to both a 66-fold increase in turnover frequency and an enhancement in oxygenate yield. By applying a combination of atomically controlled synthesis, in situ characterization, and theoretical calculations, we gain an understanding of the promoter-Rh interactions that govern catalytic performance for MoO_3-promoted Rh. We use atomic layer deposition to modify Rh nanoparticles with monolayer-precise amounts of MoO_3, with a high degree of control over the structure of the catalyst. Through in situ X-ray absorption spectroscopy, we find that the atomic structure of the catalytic surface under reaction conditions consists of Mo−OH species substituted into the surface of the Rh nanoparticles. Using density functional theory calculations, we identify two roles of MoO_3: first, the presence of Mo−OH in the catalyst surface enhances CO dissociation and also stabilizes a methanol synthesis pathway not present in the unpromoted catalyst; and second, hydrogen spillover from Mo−OH sites to adsorbed species on the Rh surface enhances hydrogenation rates of reaction intermediates.

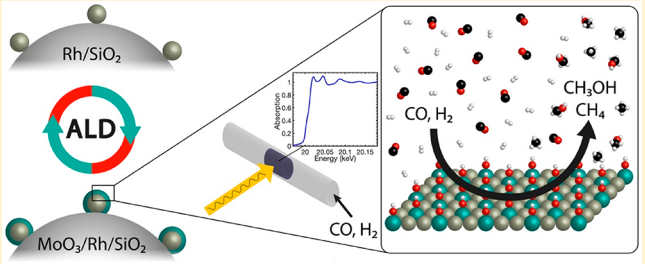

1. INTRODUCTION

The catalytic conversion of coal, natural gas, or biomass-derived synthesis gas (syngas, CO + H_2) to higher oxygenates (C_{2+} oxy) is a promising path toward the long-term production of higher value fuels and chemicals.[1−4] Rh-based catalysts are among the most widely studied for higher alcohol synthesis (HAS) due to the moderate intrinsic selectivity of Rh toward higher oxygenates.[5−13] Thermodynamic studies have determined conditions under which HAS is viable,[14] but no commercial catalyst with appropriate activity and selectivity has been developed due to the kinetically favorable side reactions that shift selectivity away from the desired products.[15,16] In particular, methanol and hydrocarbon synthesis pathways compete with C_{2+} oxy formation depending on how CO binds to the catalyst surface. Surfaces which favor CO dissociation convert syngas to hydrocarbons, whereas surfaces which allow associative CO adsorption yield methanol.[17] On Rh, the most favorable mechanism for C_{2+} oxy formation is through the insertion of CO into an alkyl fragment, a pathway which requires a coexistence of associated and dissociated CO on the catalyst surface.[7,9,18] The balance between these forms of adsorbed CO can be modified through the use of alkali and transition metal oxide promoters, which can suppress side reactions and yield improvements in activity and/or selectivity.[19−22] However, the roles of these promoters and the chemical interactions which give rise to enhanced performance are not well understood.

There are three questions regarding the Rh-promoter interactions that require more detailed investigation. First,

Received: July 13, 2019
Published: November 14, 2019

DOI: 10.1021/jacs.9b07460
J. Am. Chem. Soc. 2019, 141, 19655−19668

how does a particular promoter modify the surface structure of the catalyst? Catalyst surface structure can depend on which promoter is used, and restructuring of the catalyst during reaction can make it challenging to accurately characterize the surface structure. In some instances, a bimetallic Rh-promoter phase is claimed to form,[23,24] whereas in other cases, the promoter remains as a separate phase and the active sites are assigned to the Rh-promoter interface.[25−27] Second, how does the presence of a particular promoter affect the binding sites of key reaction intermediates to the catalyst surface? The effect of the promoter on the availability of reaction sites, adsorption energies of reactants, and location of binding sites significantly influence catalyst performance, particularly for higher alcohol synthesis, which requires adjacent associative and dissociative CO binding sites. Third, how do the surface properties and structure govern the overall catalyst performance? A better understanding of the roles different promoters play will help guide the selection of catalyst components based on the desired surface properties and catalytic reactivity.

In this work, we elucidate the role of MoO_3 in modifying the surface structure and enhancing oxygenate production over Rh catalysts. While several studies agree that MoO_3 promotion increases activity and oxygenate yield over Rh catalysts, there is disagreement on the role of the MoO_3. Kip et al. suggested that a tilted CO species adsorbs at the Rh-MoO_x interface, enabling faster CO dissociation rates.[28] The authors also hypothesized that CO may be bound directly to the molybdenum oxide promoter and could be hydrogenated to form methanol. To characterize the binding of CO to the promoted Rh surface, Szenti et al. performed temperature-programmed CO desorption measurements on 2D Rh-MoO_x films. CO desorption occurred at a higher temperature on the Rh-MoO_x surfaces, leading the authors to conclude that strongly bound CO species were present at the Rh-MoO_x interface.[29] On the other hand van den Berg et al. suggested that hydrogenation was the rate-limiting step on Rh-MnO-MoO_2/SiO_2, and the increased activity was due to greater surface coverage of hydrogen at the expense of CO.[30] In their study, however, the effects of MoO_2 were not isolated from MnO, which has been shown to significantly promote oxygenate production.[31−33] Recently, Zhang et al. reported an increase in methanol production over Rh nanoparticles on a MoO_3-modified silica support.[34] The authors reported an increase in the proportion of adsorbed gem-dicarbonyl species on the catalyst with MoO_3 present, suggesting that these sites may be responsible for enhanced methanol yield. However, the authors observed differences in Rh nanoparticle size on the supports with and without MoO_3 modification, which could not be deconvoluted from the effects of the MoO_3.

The chemical state and structure of the MoO_3-modified Rh catalyst is also still under question. Although all these studies agree that the MoO_3 promoter is reduced at high temperature in hydrogen, the oxidation state of Mo during reaction remains unclear. Kip et al. suggested reduction of Mo^{6+} to Mo^{2+} based on hydrogen consumption during temperature-programmed reduction experiments. On the other hand, Zhang et al. performed XPS measurements following catalyst reduction, taking care to prevent exposure of the catalyst to air, and claimed reduction of Mo^{6+} to Mo^0. Neither study examined changes in Mo oxidation state in syngas following catalyst reduction. Kip et al. and van den Berg et al. observed decreased CO adsorption on the promoted Rh surface, and suggested that the molybdenum oxide likely sits on top of the Rh particles. However, the structure of the molybdenum oxide on the catalyst surface could not be directly determined from these CO chemisorption measurements. In all these studies, the lack of in situ characterization leaves the structure and oxidation state of the catalyst under reaction conditions unclear.

In this work, we promote Rh nanoparticles on silica with controlled monolayer amounts of MoO_3 deposited by atomic layer deposition (ALD). The self-limiting nature of the ALD process enables the design and synthesis of promoted catalysts with atomic-level precision.[35−40] Furthermore, the promotional effects of MoO_3 can be isolated from variations in nanoparticle size and shape that may arise from other synthesis methods. Through syngas conversion reactions and computational modeling, we show that MoO_3 promotion leads to significantly enhanced activity and greater selectivity toward methanol at the expense of hydrocarbons. We use CO chemisorption, diffuse reflectance infrared Fourier transform spectroscopy (DRIFTS), and density functional theory (DFT) to analyze the interactions between MoO_3 and adsorbed CO. The structure of the catalyst is studied using in situ X-ray absorption spectroscopy (XAS), from which we determine that Mo−OH species are substituted into the surface of the metallic Rh nanoparticles under reaction conditions. On the basis of the structure of the surface and the catalytic performance, we identify two roles of MoO_3: (1) to stabilize OH binding, resulting in increased CO dissociation and providing a pathway for methanol formation via $*CH_xO$ species and (2) to increase hydrogenation rate of reaction intermediates.

2. EXPERIMENTAL AND THEORETICAL METHODS

2.1. Catalyst Synthesis. All catalysts were prepared on silica gel (Davisil grade 643, Sigma-Aldrich). Because catalyst performance is strongly susceptible to impurities,[22,41] the silica gel was washed in 2 M nitric acid at 80 °C for 2 h to remove alkali and transition metal contaminants. Excess nitric acid was removed by rinsing the silica with Milli-Q water until a neutral pH was obtained, and the powder was dried in air at 120 °C for 24 h. To avoid structural changes in the silica support during calcination of the sample in subsequent steps, the washed silica gel was calcined in air at 550 °C for 4 h. Rh nanoparticles were prepared on the silica gel with a weight loading of 5% by incipient wetness impregnation (IWI) of an aqueous $RhCl_3 \cdot xH_2O$ solution (39% Rh, Sigma-Aldrich). The powder was held under vacuum for 2 h prior to Rh IWI to evacuate the pores and the Rh solution was added dropwise while constantly stirring. The powder was dried for 24 h, then calcined in air at 500 °C for 4 h to produce Rh_2O_3 nanoparticles. A 1 wt % MoO_3 catalyst was prepared on the washed, calcined silica support by incipient wetness impregnation of the appropriate mass of ammonium heptamolybdate tetrahydrate ($(NH_4)_6Mo_7O_{24} \cdot 4H_2O$, Sigma-Aldrich).

MoO_3 was deposited onto the powders by atomic layer deposition in a custom-built reactor at 160 °C. Powders were pretreated in ozone to functionalize the surface. In each ALD cycle, the sample was exposed to $Mo(CO)_6$ (Sigma-Aldrich) for 35 s (5 s pulse time, 30 s soak time) and O_3 for 5 s, and the precursors were purged from the reactor with N_2 for 60 s between each dose. The $Mo(CO)_6$ precursor was held at 40 °C and the delivery line was heated to 55 °C to ensure adequate vapor pressure of $Mo(CO)_6$. The O_3 was formed from O_2 by an AC-2025 ozone generator (In USA Inc.), yielding a feed gas composition of 10% O_3/90% O_2. Powders were contained in a custom particle holder built following the design of Libera et al.[42]

To differentiate the various catalysts, the following nomenclature will be used in this article. "Rh" will refer to 5 wt % Rh deposited on SiO_2 gel by IWI. "MoO_3" will refer to 1 wt % MoO_3 prepared on SiO_2 gel by IWI. We will use "NMoO$_x$/Rh" to indicate N ALD cycles of molybdenum oxide deposited on the Rh catalyst. Finally, "NMoO$_x$"

DOI: 10.1021/jacs.9b07460
J. Am. Chem. Soc. 2019, 141, 19655−19668

will be used to indicate N ALD cycles of molybdenum oxide deposited on the bare silica support, without Rh present. We have used values of N varying between 1 and 100. We will show that the oxidation state of Mo depends on the environment of the catalyst, so in each section we will specify the value of x in MoO_x.

2.2. Catalytic Testing and CO Chemisorption. Catalytic reactivity was tested using an Altamira Benchcat 4000 HP packed bed reactor. Catalysts were loaded into a 1/4 in. outer diameter stainless steel tube with a chemically inert coating (Silcolloy). The catalytic performance was tested under low and high CO conversion conditions. In a typical low CO conversion experiment, 27 mg of catalyst was diluted with 50 mg of silica gel and packed between two plugs of quartz wool. For high CO conversion experiments, the catalyst mass was increased to 90 mg, and 70 mg silica gel was used for dilution. The catalyst bed was held in place on both sides by glass beads. Catalysts were reduced in H_2 (Airgas, 5.0 purity) at 250 °C for 2 h. After raising the pressure to 20 bar in N_2, the feed gas was switched to syngas (H_2:CO = 2:1), with a total flow rate of 60 sccm for low conversion experiments, and 15 sccm for high conversion experiments, and catalytic performance was measured for 36 h at 250 °C and 20 bar. The CO (Airgas, 5.0 purity) was passed through alumina pellets at 300 °C and a room temperature bed of carbon black (Vulcan XC-72) to remove metal carbonyls. The temperature, pressure, and gas flow rates were identical across all catalysts so that the performance could be compared under a fixed set of conditions. Reaction products were separated by an Agilent 7890B gas chromatograph−mass spectrometer and quantified by a flame-ionization detector. The ratio of the total carbon content in all products to the CO concentration in the feed was used to calculate the percentage of CO converted. This percentage was converted to a reaction rate based on the CO flow rate, and the activity was normalized to the mass of the catalyst. Carbon-weighted selectivities were calculated by dividing the total number of carbon atoms in a given product by the total number of carbon atoms in all products.

Temperature-programmed reduction (TPR) and CO chemisorption experiments were performed using an Altamira Hybrid Chemisorption-Reactor system. In a typical experiment, 50−60 mg of catalyst powder was loaded into a quartz U-shaped tube between two quartz wool plugs. Catalysts were heated to 300 °C under He flow to remove excess water. After cooling to 40 °C, temperature-programmed reduction experiments were performed by ramping the temperature of the catalyst at 10 °C/min to 500 °C and holding for 30 min in a 10% H_2/90% Ar mixture. The reduction of the catalyst was monitored by a thermal conductivity detector (TCD). CO chemisorption experiments were then carried out at 30 °C on the reduced catalyst. A known volume of 10% CO/90% He mixture was pulsed over the catalyst and the effluent gas was analyzed by a TCD. The amount of CO adsorbed on the catalyst was quantified by integrating the TCD signal. The catalyst was exposed to repeated pulses of CO until no change in the TCD peak area was observed, indicating saturation of the catalyst surface.

2.3. Ex Situ Catalyst Characterization. Transmission electron microscopy (TEM) was performed on an FEI Tecnai G2 F20 X-TWIN TEM system operated at 200 kV. Samples were prepared by dispersing the catalyst powder in ethanol and drop casting on lacey carbon/copper TEM grids (Ted Pella). Scanning TEM and energy-dispersive X-ray spectroscopy (STEM-EDS) elemental mapping was performed using an EDAX super ultrathin window (SUTW) and analyzer.

Inductively coupled plasma mass spectrometry (ICP-MS) was performed on a Thermo Scientific XSERIES 2 Quadrupole ICP-MS instrument. To prepare samples, ∼10 mg of catalyst was dissolved in boiling aqua regia for 3 h, then diluted with Milli-Q water. Rh and Mo standard solutions (Sigma-Aldrich) were diluted to three different concentrations with 3% aqua regia for calibration.

X-ray photoelectron spectroscopy (XPS) measurements were performed using a PHI VersaProbe III with Al Kα radiation (1486.6 eV). Pass energies of 224.0 and 55.0 eV were used for survey and high-resolution scans, respectively. Samples were prepared by pressing the powders into carbon tape, attached to a Si wafer. Dual electron and ion neutralization were used during measurement to mitigate charging effects and all binding energies were normalized to the position of the Si 2p peak at 103.5 eV. To maximize signal-to-noise, a spot size of 1400 μm × 100 μm with high power setting was used (100 W, 18 kV).

X-ray diffraction was performed at beamline 2−1 at Stanford Synchrotron Radiation Lightsource (SSRL). A Si(111) double-crystal monochromator was used to set the X-ray energy to 15.5 keV (λ = 0.800 Å). Diffraction patterns were collected by a Pilatus 100k detector. Each sample was packed into a quartz glass capillary and held in place by a plug of quartz wool. The diffraction pattern for the bare Si support was subtracted from that of each sample, yielding the pattern for the catalyst only.

2.4. In Situ Catalyst Characterization. Diffuse reflectance infrared Fourier transform spectroscopy (DRIFTS) was performed in a Praying Mantis DRIFTS system (Harrick). Samples were loaded into a high temperature and high pressure reaction cell with ZnSe windows. Gas flow rates were controlled using EL-Flow series mass flow controllers (Bronkhorst). CO was passed through a bed of alumina pellets at 300 °C to decompose iron and nickel carbonyl impurities. Measurements were performed at 1 atm and pressures were monitored using a pressure transducer (Setra). IR spectra were measured using a Bruker Vertex 70 spectrometer with a liquid nitrogen-cooled mercury-cadmium-telluride (MCT) detector. In a typical experiment, samples were heated to 250 °C at 5 °C/min in H_2 and held for 2 h to reduce the catalysts. Background IR spectra were then collected at room temperature in N_2. Catalysts were exposed to CO at 1 atm and room temperature until the surface was saturated with adsorbed CO. Excess CO was purged from the cell and spectra were collected under N_2 to reduce the signal from gas phase CO.

X-ray absorption spectroscopy (XAS) was performed on beamlines 2−2 and 4−1 at SSRL. Each sample was packed in a 1 mm OD quartz glass tube with wall thickness 20 μm between two plugs of quartz wool, which was loaded into a custom-built high temperature and pressure reactor described previously.[43] Unlike the reactivity tests, the catalyst was not diluted with silica gel in order to achieve an optimal edge step and high signal-to-noise ratio in the XAS data. Gas flow rates were controlled using mass flow controllers (Brooks) and CO was purified using a Nanochem Metal-X purifier (Matheson) to remove metal carbonyls. Pressure was controlled using a back-pressure regulator (Swagelok). Temperature was controlled using a Eurotherm PID controller and monitored with a K-type thermocouple in the catalyst bed.

X-ray absorption near edge structure (XANES) and extended X-ray absorption fine structure (EXAFS) measurements were performed at the Rh K-edge (23 220 eV) and Mo K-edge (20 000 eV). Incident photon energy was set by step-scanning the Si (220) (crystal orientation φ = 0) double-crystal monochromator. XAS data was collected in transmission mode using Ar-filled ionization chambers, with simultaneous measurement of Rh or Mo foils for energy calibration. Four replicates of each EXAFS spectrum were collected and merged to ensure a high signal-to-noise ratio.

In a typical experiment, EXAFS scans were first performed with the catalyst at room temperature and under He flow to characterize the as-prepared state of the catalyst. Catalysts were then reduced by ramping the temperature to 250 °C in H_2. XANES scans were collected every 11 min, alternating between the Rh and Mo K-edges, to monitor the state of the catalyst during reduction, and the reduction was judged to be complete when consecutive XANES scans were identical. EXAFS spectra were then collected at 250 °C in H_2 to characterize the structure of the reduced catalyst. The cell pressure was subsequently increased to 20 bar in H_2 and the gas feed was switched to syngas (H_2:CO = 2:1). XANES measurements alternating between the Rh and Mo K-edges were performed to monitor the structural evolution of the catalyst in syngas. Once consecutive XANES spectra showed no change, EXAFS measurements were performed at 250 °C in 20 bar syngas to characterize the steady-state structure of the catalyst under reaction conditions.

Initial processing and analysis of the XAS data was performed using the Athena software of the Demeter package.[44] The replicate XAS

DOI: 10.1021/jacs.9b07460
J. Am. Chem. Soc. 2019, 141, 19655−19668

spectra were aligned, merged, energy calibrated, and normalized. Linear combination fitting of the XANES data was attempted for each measurement. Rh metal foil and Rh_2O_3 were used as standards for analyzing Rh XANES, while Mo metal foil, MoO_3, Na_2MoO_4, $(NH_4)_6Mo_7O_{24}{\cdot}4H_2O$ (AHM), MoO_2, Mo_2C, $MoSi_2$, and $Mo(CO)_6$ were used as standards for analyzing Mo XANES.

Detailed modeling of the EXAFS data was performed in the Artemis software of the Demeter package.[44] Models were built from absorber-backscatter scattering paths, simulated from bulk material crystallographic data using FEFF6. S_0^2 was determined by modeling the Rh and Mo foil EXAFS, and found to be 0.85 for Rh (Figure S1, Table S1) and 0.81 for Mo (Figure S2, Table S2). Models of the catalyst EXAFS were optimized in R-space using k^1, k^2, and k^3 weightings with all models obeying the Nyquist criterion.[45] Fourier transformation was performed on the k^3-weighted EXAFS function (k = 3−14 Å^{-1} for Rh; k = 3−13 Å^{-1} for Mo) and fitting was performed on an R-range of 1.0−3.3 Å for Rh and 1.3−3.2 Å for Mo. Scattering paths generated from Rh_2O_3 and AHM crystallographic data were used to model the Rh and Mo EXAFS for the as-prepared catalysts. The Rh K-edge EXAFS of the catalyst postreduction and under steady-state reaction conditions were simultaneously modeled using backscattering paths from bulk *fcc* Rh metal. The structure of Mo postreduction was modeled using a Mo−Rh backscatter path generated by replacing a Rh atom with Mo in the *fcc* Rh lattice. This backscattering path, along with a Mo−O scattering path from bulk $MoRh_2O_6$ were used to model the Mo EXAFS under steady-state reaction conditions. The Mo EXAFS of the catalyst during reaction was also modeled using Mo−O and Mo−Rh scattering paths from the DFT-optimized structure.

2.5. Computational Methods. The theoretical XANES simulations were performed using FEFF,[46,47] using clusters with SCF and FMS cutoff radii of 5 and 9 Å, respectively. These clusters were generated using available experimental crystal structures in all cases except for the catalyst in its reaction state, where the DFT-optimized structure was used. All systems were simulated using the standard Hedin−Lundqvist self-energy. Finally, thermal disorder was accounted for by using the single-scattering, correlated Debye model approximation using experimental or estimates of the Debye temperatures.

Electronic structure calculations were performed using the Quantum ESPRESSO software package,[48] implemented in the Atomic Simulation Environment (ASE).[49] The Bayesian error estimation functional with van der Waals correlation (BEEF-vdW) was used to accurately model adsorption energies and van der Waals interaction.[50] In all calculations, plane wave and density wave cutoffs of 500 and 5000 eV, respectively, were used, along with a 4 × 4 × 1 Monkhorst−Pack k-point grid.[51] A four layer (3 × 3) *fcc* Rh(111) slab was used in the calculations and the top two layers were allowed to relax during the geometric optimizations until the force on each atom was less than 0.03 eV/Å. The slabs were separated by 15 Å of vacuum in the *z*-direction. All the possible surfaces have been considered with Rh atoms substituted by MoO_xH_y.

All adsorption and transition state energies were calculated from DFT as the electronic energy of the adsorbate on top of a slab minus the combined electronic energies of the empty slab and the associated gas phase reference molecules (CO, H_2, and H_2O). Energies were then used as inputs into the CatMAP software.[52] The reaction network has been described previously[53] so we will briefly summarize here. The C−O bond dissociation reactions occur via either the CHOH* or CH_3O* intermediate, which result in CH* or CH_3* on the surface, respectively. The model considers methane formation through the hydrogenation of both of these intermediates. The formation of ethanol and acetaldehyde occurs via CO insertion into CH* or CH_3*, and subsequent hydrogenation. Finally the model considers methanol formation pathways by the hydrogenation of CHOH* and CH_2O*. On the basis of this reaction network, formation rates of each product can be expressed in terms of the adsorption and transition state energies of each intermediate and elementary reaction step. Using linear scaling relations, between adsorption and transition state energies of different intermediates, the formation rate of each product can be expressed in terms of two descriptors: the CO and OH adsorption energies. Activity heatmaps corresponding to rates as functions of the CO and OH descriptor adsorption energies were generated from the simplified product formation rate expressions. Electronic energy differences were converted to free energies in CatMAP by adding corrections for zero-point energy (ΔZPE) and entropy ($-T\Delta S$) (in the harmonic approximation for adsorbates and using ideal gas thermochemistry as implemented in ASE).

3. RESULTS AND DISCUSSION

3.1. Catalyst Performance. The syngas conversion activity and selectivity of unpromoted and MoO_3-promoted Rh catalysts are shown in Figure 1 and Table 1. The

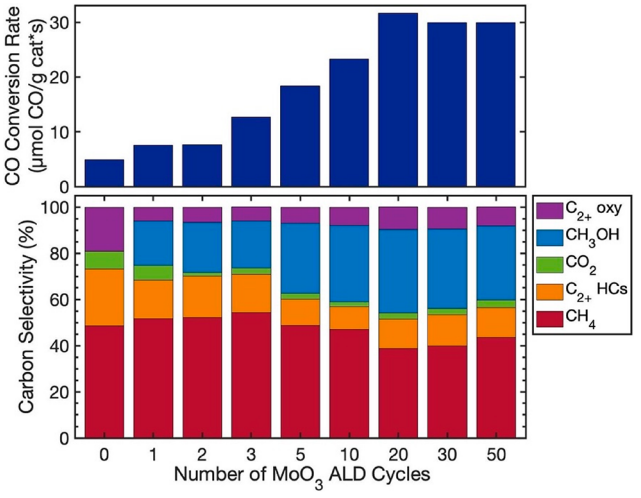

Figure 1. Steady state syngas conversion activity and selectivity of MoO_3-promoted Rh catalysts as a function of MoO_3 ALD cycles. All reactions were carried out at T = 250 °C, P = 20 bar, total flow rate of 60 sccm (H_2:CO = 2:1). C_{2+} HC represents higher hydrocarbons and C_{2+} oxy represents higher oxygenates.

unpromoted Rh catalyst shows high selectivity toward methane and higher hydrocarbons, with a small yield of higher oxygenates. The oxygenates are primarily acetaldehyde and ethanol, in a 16:1 ratio, with C_{3+} oxygenates being trace products (Table S3). This performance is in good agreement with prior studies.[7,54] After 1 ALD cycle of MoO_3 there is a marked shift in selectivity toward methanol production, with a corresponding decrease in selectivity to C_{2+} hydrocarbons. As the MoO_3 loading increases up to 20 ALD cycles, the methanol selectivity increases, while methane and higher hydrocarbon selectivities decrease. The distribution of higher oxygenates shifts to >97% ethanol and no acetaldehyde is detected. Over this range of MoO_3 loading, the CO conversion rate monotonically increases, reaching 6.5 times that of the unpromoted Rh. The increase in catalyst activity outpaces the slight decrease in higher alcohol selectivity, so that the $20MoO_x$/Rh catalyst has a 3.2-fold increase in higher alcohol yield compared to unpromoted Rh.

There are several trends in the activity and selectivity that demonstrate an increased rate of hydrogenation of reaction intermediates on the MoO_3-promoted Rh catalysts. We describe in turn each piece of evidence that supports faster hydrogenation. First, the enhanced methanol production can be explained by the rapid hydrogenation of associated CO directly to methanol. Second, the addition of MoO_3 increases

DOI: 10.1021/jacs.9b07460
J. Am. Chem. Soc. 2019, 141, 19655−19668

Table 1. Steady State Syngas Conversion Performance of MoO_3-Promoted Rh Catalysts[a]

number of MoO_3 ALD cycles	carbon selectivity (%)					% CO converted	reaction rate (μmol CO/g·s)
	CH_4	C_{2+} HC	CO_2	MeOH	C_{2+} oxy		
0	48	25	8	0	19	1.1	4.9
1	52	17	6	19	6	1.4	7.6
2	52	18	1	22	7	1.4	7.7
3	54	17	3	20	6	3.0	12.7
5	49	11	3	30	7	3.9	18.3
10	47	10	2	33	8	5.6	23.3
20	39	13	3	36	9	5.7	31.7
30	40	13	3	34	10	5.8	30.0
50	44 ± 2	13 ± 2	3 ± 0.4	32 ± 3	8 ± 0.7	5.7 ± 0.2	30.0 ± 1.4

[a]Measurements performed at 250 °C, 20 bar Syngas, 60 sccm total flow rate (H_2:CO = 2:1). C_{2+} HC represents higher hydrocarbons and C_{2+} oxy represent higher oxygenates. Uncertainties shown are standard deviations across four replicate experiments.

Table 2. CO Chemisorption on ALD MoO_3-Promoted Rh Catalysts[a]

number of MoO_3 ALD cycles	reaction rate (μmol/g·s)	CO uptake (μmol/g)	TOF (s^{-1})
0	4.9	104 ± 8	0.048
1	7.6	84	0.091
2	7.7	67	0.11
3	12.7	72	0.18
5	18.3	55	0.33
10	23.3	36	0.64
20	31.7	14	2.23
30	30.0	9	3.19
50	30.0	11	2.68

[a]Uncertainty is one standard deviation, measured across four replicate experiments. Measurements performed at 30 °C, 1 atm.

the ratio of methane to C_{2+} hydrocarbon production, which can be understood by examining the reaction pathways leading to each product. Following CO dissociation, formation of higher hydrocarbons through C−C coupling competes with CH_x hydrogenation to methane; the selectivity to C_{2+} hydrocarbons decreases much more significantly than that of methane, suggesting that the faster rate of hydrogenation outcompetes the C−C coupling pathway. Third, among the higher oxygenates, Rh produces primarily acetaldehyde, whereas this product is fully hydrogenated to ethanol on the MoO_3-promoted Rh catalysts. Finally, an enhancement in hydrogenation kinetics may increase the turnover of species on the surface, leading to higher activity. It is worth noting, however, that an enhanced hydrogenation rate may not be sufficient to explain the higher rate of production of all the reaction products observed, since hydrogenation may not be a rate-limiting step in all reaction pathways.

As the MoO_3 loading increases beyond 20 ALD cycles, methanol selectivity decreases slightly in favor of methane, and the reaction rate decreases somewhat as well. We propose that with significant MoO_3 covering the catalyst, the promotional effects are offset by a loss in reaction sites due to a physical blocking effect. It is expected that CO conversion will continue to drop with increasing MoO_3 ALD cycles beyond 50 as the Rh nanoparticles become fully encapsulated by MoO_3.

Additional catalytic performance testing was done with a higher catalyst mass and a lower syngas flow rate to determine if the same trends in activity and selectivity existed at higher CO conversion conditions (Table S4). As with the low conversion tests, the overall CO conversion rate increases significantly as the number of MoO_3 ALD cycles increases. Under high CO conversion conditions, catalysts with 10 or fewer MoO_3 ALD cycles showed similar methanol and higher oxygenate selectivity to the low conversion tests. These catalysts showed a slight increase in selectivity toward higher hydrocarbons at the expense of methane, but the total selectivity toward all hydrocarbons was nearly identical to the low conversion tests. For catalysts with 20 or more MoO_3 ALD cycles, the percent CO conversion values are significantly higher than in the low conversion tests. The product selectivity for these catalysts shifts toward methane production instead of the methanol observed under low conversion conditions. We expect that under the high CO conversion conditions, there are significant secondary reactions, leading to the formation of methane, the most thermodynamically favorable product.

To better understand the origin of the improved CO hydrogenation activity resulting from addition of MoO_3, we quantified the CO chemisorption on the MoO_3-promoted Rh catalysts (Table 2). Surprisingly, the CO uptake decreases dramatically as the MoO_3 loading increases. The catalysts modified with 20 or more ALD cycles of MoO_3 show an order of magnitude decrease in CO uptake relative to unpromoted Rh. The CO conversion rate was divided by the CO uptake to estimate turnover frequency (TOF). The combination of enhanced activity even as CO uptake decreases implies significantly enhanced TOFs in the promoted catalysts, as confirmed by the TOF values in Table 2. For instance, compared to unpromoted Rh, the 30MoO_x/Rh catalyst has a 6.1 times higher reaction rate, but a 66-fold increase in TOF. It is important to note here that the ALD process does not alter the Rh nanoparticle size or shape (Figure 2), so variations in CO chemisorption can be attributed purely to the blocking of CO adsorption sites by MoO_3. The results therefore show that while MoO_3 covers the Rh nanoparticles and blocks reaction sites, it significantly enhances the reaction rate on the remaining sites.

3.2. Catalyst Characterization. *3.2.1. As-Prepared Catalysts.* Physical characteristics of the catalysts were studied by TEM. Average nanoparticle diameters were measured from TEM images and found to be ∼4 nm (Figure 2) for both the Rh and 5MoO_x/Rh catalysts. The presence of contaminants in the as-prepared catalysts was assessed by XPS. The survey scan of the Rh catalyst shows peaks corresponding to Rh, Si, O, and C (Figure S3). The survey of the 50MoO_x/Rh catalyst shows these elements as well as Mo. A small Cl peak is observed in both catalysts in the as-prepared state, suggesting that a small amount of Cl remains on the catalyst from the $RhCl_3$

DOI: 10.1021/jacs.9b07460
J. Am. Chem. Soc. 2019, 141, 19655−19668

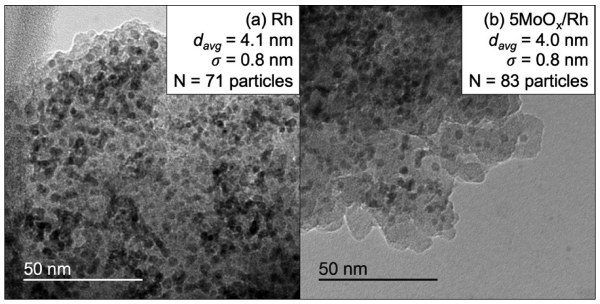

Figure 2. Bright-field TEM images of (a) Rh and (b) 5MoO$_x$/Rh catalysts in the as-prepared state. Average nanoparticle sizes and standard deviations were calculated from the measured diameters of the specified number of nanoparticles.

precursor. However, this peak vanishes in the survey scans measured postreaction, and it is likely that the residual Cl is removed during catalyst reduction[55] and does not affect the reactivity. Spectroscopic characterization of Rh in the as-prepared catalysts using a combination of XPS, XANES, and EXAFS supports a Rh^{3+} oxidation state, consistent with the expected Rh_2O_3. The Rh 3d binding energies for several of the as-prepared catalysts measured by XPS are consistent with the Rh^{3+} oxidation state and fits to the data indicate that no other Rh oxidation states are present; a representative spectrum is shown in Figure S4 for the 50MoO$_x$/Rh catalyst. A detailed in situ EXAFS study was performed on the 20MoO$_x$/Rh catalyst, since this catalyst showed the greatest increase in activity and oxygenate selectivity compared to unpromoted Rh. The Rh K-edge XANES of this catalyst in the as-prepared state has features similar to that of Rh_2O_3 (Figure 3a) consistent with an oxidic form of Rh. Similarly, the Rh K-edge EXAFS of this catalyst in the as-prepared state shows Rh−O scattering paths, consistent with the oxidized Rh observed by XPS (Figures 3b, S5, Table S1). Next-nearest neighbor Rh−Rh scattering is very weak, and no scattering from higher order shells is observed, suggesting disorder in the as-prepared catalyst beyond nearest-neighbor bonds. XRD measurements show no crystalline features in the as-prepared catalyst, corroborating the lack of order seen in EXAFS (Figure S6).

The Mo in the as-prepared catalyst is fully oxidized to Mo^{6+} (x = 3 in MoO$_x$). As with Rh, the Mo 3d region of the XPS spectrum shows a single pair of peaks, with binding energy consistent with Mo^{6+} across all the catalysts measured; a representative spectrum for the 50MoO$_x$/Rh catalyst is shown in Figure S4. The shape of the Mo K-edge XANES spectrum strongly depends on the oxidation state and the bonding geometry around the Mo atom.[56,57] The Mo K-edge XANES of the sample was compared with bulk MoO_3 and $(NH_4)_6Mo_7O_{24}{\cdot}4H_2O$ (AHM), which have slightly distorted octahedral configurations of O atoms around each Mo, as well as Na_2MoO_4, in which each Mo atom is 4-fold coordinated with O atoms in a tetrahedral geometry (Figures 4, S7). The pre-edge peak seen in the catalyst sample and all 3 standards is characteristic of Mo^{6+}, but the intensity closely matches that of the distorted octahedral Mo geometry in AHM rather than that in MoO_3. Furthermore, the overall shape of the XANES region follows that of AHM much more closely than bulk MoO_3. This suggests that the local structure of the Mo deposited by ALD better resembles that of the slightly distorted six coordinate Mo−O structure in AHM rather than the more highly distorted 6-fold coordinated structure in bulk MoO_3. The results of the as-prepared Mo EXAFS modeling show several nearest-neighbor Mo−O bond lengths consistent with an oxidic form of molybdenum (Figures 4, S8, Table S2). Scattering from higher order shells is weak, suggesting a lack of long-range order, consistent with the XRD characterization of the as-prepared catalyst (Figure S6) as well as previous reports of amorphous MoO_3 grown by ALD.[58,59]

The weight loading of molybdenum was measured by inductively coupled plasma mass spectrometry (ICP-MS) and is presented in Table 3 and Figure S9. The Mo weight loading increases with the number of ALD cycles on powders with and without Rh present, but samples with Rh show 4−5 orders of magnitude higher Mo loading than those without Rh. This difference in growth implies either an inherently greater reactivity of the $Mo(CO)_6$ precursor with the Rh_2O_3

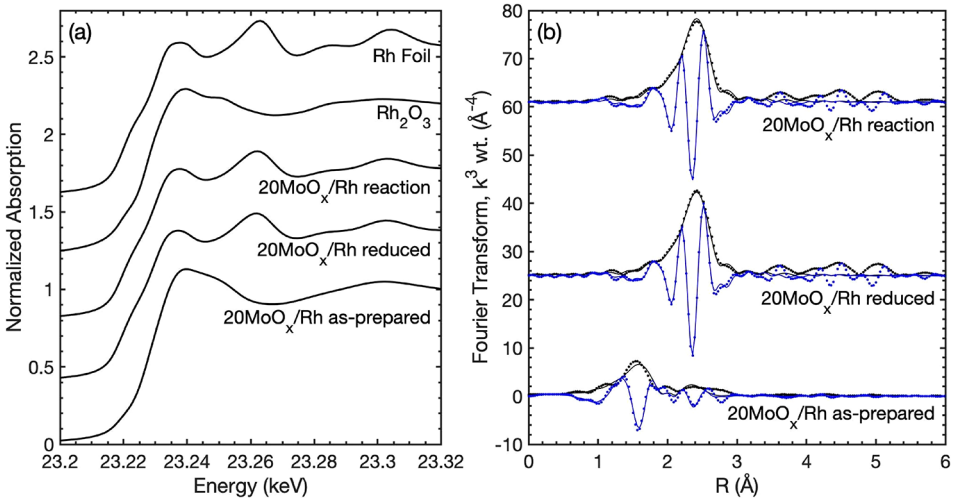

Figure 3. In situ Rh K-edge XAS of 20MoO$_x$/Rh catalyst. Measurements are shown for the catalyst in as-prepared (20 sccm He, 1 atm, 25 °C; x = 3), reduced (20 sccm H_2, 1 atm, 250 °C; x = 0), and reaction (20 sccm H_2, 10 sccm CO, 20 bar, 250 °C; x = 1) conditions. (a) XANES region is shown for the catalyst and bulk Rh_2O_3 and Rh foil standards. (b) Magnitude (black) and imaginary component (blue) of the EXAFS Fourier transform are shown. Measured data are shown as points and fits are shown as solid lines. Catalyst spectra were fit in an R range of 1.0−3.3 Å. Spectra are offset for clarity. Corresponding k-space EXAFS and table of EXAFS fitting results are shown in Figure S5 and Table S1.

DOI: 10.1021/jacs.9b07460
J. Am. Chem. Soc. 2019, 141, 19655−19668

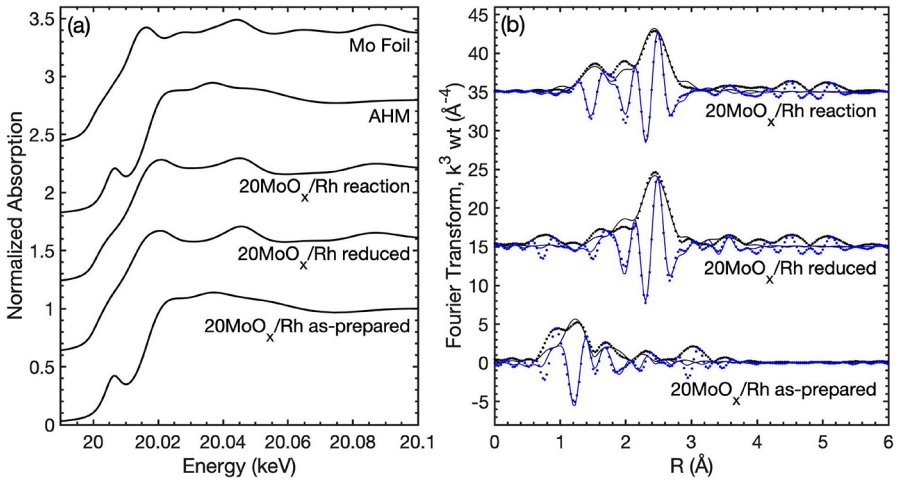

Figure 4. In situ Mo K-edge XAS of 20MoO$_x$/Rh catalyst. Measurements are shown for the catalyst in as-prepared (20 sccm He, 1 atm, 25 °C; x = 3), reduced (20 sccm H_2, 1 atm, 250 °C; x = 0), and reaction (20 sccm H_2, 10 sccm CO, 20 bar, 250 °C; x = 1) conditions. (a) XANES region is shown for the catalyst and bulk ammonium heptamolybdate tetrahydrate (AHM) and Mo foil standards. (b) Magnitude (black) and imaginary component (blue) of the EXAFS Fourier transform are shown. Measured data are shown as points and fits are shown as solid lines. Catalyst spectra were fit in an R range of 1.3−3.2 Å. Spectra are offset for clarity. Corresponding k-space EXAFS and table of EXAFS fitting results are shown in Figure S8 and Table S2.

Table 3. Mo Loading on Catalysts with and without Rh Measured by ICP-MS

number of MoO_3 ALD cycles	wt % Mo with Rh	wt % Mo without Rh
0	6.5×10^{-6}	–
5	0.25	2.6×10^{-5}
10	0.43	3.4×10^{-5}
20	1.14	7.6×10^{-5}
50	1.93	2.1×10^{-4}

nanoparticles or a preference of $Mo(CO)_6$ to react at the highly undercoordinated sites on the nanoparticles surface, and strongly suggests that the MoO_3 promoter was selectively deposited on the Rh nanoparticles.

To support this hypothesis, the distribution of Si, Rh, and Mo atoms was mapped by STEM-EDS and is presented in Figure 5. Correlation coefficients between the locations of each pair of elements were calculated to be 0.49 (Rh−Si), 0.59 (Mo−Si), and 0.66 (Rh−Mo). The correlation coefficient between two elements would have a value of −1 if the elements were never located in the same position, 1 if the elements were perfectly colocated, and 0 if the locations of the elements were completely independent. As expected, all of the correlation coefficients are greater than 0 because the Rh and Mo are supported on the SiO_2. For a uniform deposition process, the distribution of Mo atoms would be expected to be highly correlated with that of Si, with an expected Mo−Si correlation coefficient of 1. However, we find that the distribution of Mo atoms is more highly correlated with that of Rh than Si, consistent with the selective deposition of MoO_3 on the Rh_2O_3 nanoparticles. An important consequence of the selective deposition of MoO_3 on the Rh_2O_3 nanoparticles is that the characterization of Mo in our catalysts discussed later reflects catalytically relevant Mo in close contact with Rh. This proximity of Rh and Mo will enable us to determine the structure of the catalyst surface and the role of MoO_3 in promoting CO hydrogenation.

3.2.2. Reduced Catalyst. Rh K-edge XANES measurements following the exposure of the 20MoO$_x$/Rh catalyst to hydrogen at 25 °C show that the Rh_2O_3 nanoparticles become

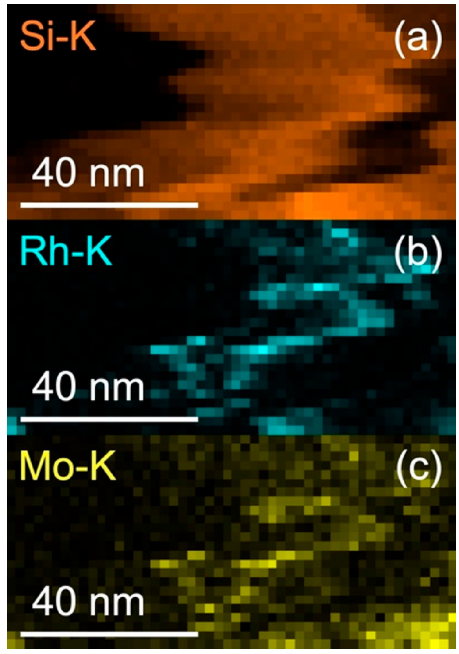

Figure 5. STEM-EDS elemental maps of (a) Si, (b) Rh, and (c) Mo for 50MoO$_x$/Rh catalyst in the as-prepared state.

reduced to a metallic state (Figure S10). The room temperature reduction of Rh_2O_3 was somewhat unexpected, as TPR measurements showed the Rh reduction peak at 80 °C (Figure S11), in agreement with literature.[60] There are no significant changes in the Rh XANES as the catalyst temperature increases to 250 °C. The Rh K-edge EXAFS of the fully reduced catalyst at 250 °C was modeled using an *fcc* metallic Rh structure (Figures 3, S5, Table S1). The first-shell coordination number (CN) is 9.9 ± 0.4, less than the value of 12 expected for a bulk *fcc* metal. This reduced CN is consistent with having nanoparticles, for which the surface atoms are undercoordinated.[61] Inclusion of Rh−O scattering paths in the model worsened the quality of the fit, confirming that there is

DOI: 10.1021/jacs.9b07460
J. Am. Chem. Soc. 2019, 141, 19655−19668

no residual rhodium oxide present in the reduced catalyst (Table S5).

As with the Rh_2O_3, the MoO_3 also substantially reduces upon high temperature hydrogen exposure. The TPR profile of the $10MoO_x$/Rh catalyst shows an additional reduction peak at 230 °C that is not present for unpromoted Rh (Figure S11). The reduction of MoO_3 at this low temperature is highly unusual for supported molybdenum oxide species,[62,63] as confirmed by TPR experiments of the MoO_3 catalyst without Rh present, which shows no reduction at temperatures below 400 °C (Figure S11). The reduction of MoO_3 was further analyzed by in situ TPR-XANES of the $20MoO_x$/Rh catalyst. Upon exposure to hydrogen at room temperature, the MoO_3 substantially reduces, as seen by the loss of the pre-edge feature (Figure S12). As the temperature increases to 250 °C, further reduction of the molybdenum oxide occurs, indicated by a decrease in the Mo K-edge energy. The presence of isosbestic points in the Mo TPR-XANES shows a one-to-one transformation as the molybdenum oxide is reduced, and linear combination fits of each XANES spectrum during reduction could be achieved using the first and last scans as standards (Figure S13). However, it was not possible to obtain satisfactory linear combination fitting of the reduced sample Mo K-edge XANES with any of the bulk references, MoO_3, Na_2MoO_4, AHM, MoO_2, and Mo metal. Surprisingly, the R-space Mo EXAFS in the reduced catalyst closely resembled that of *fcc* Rh, rather than metallic *bcc* Mo, for which the peak at R∼2.9 Å is not present in the catalyst Mo EXAFS (Figures 4, S2). This suggests that Mo atoms are incorporated into the metallic *fcc* Rh lattice during catalyst reduction. We therefore modeled the metallic scattering features in the Mo EXAFS of the reduced catalyst using a Mo atom substituted into the *fcc* Rh lattice (Figures 4, S8, Table S2), which resulted in an excellent fit to the data using only this single scattering path (x = 0 in MoO_x). The relatively large undercoordination of the Mo−Rh scattering path (CN = 8.3 ± 0.8) suggests that the molybdenum is primarily a surface species. In particular, if Mo were sitting on top of the Rh surface as an adatom, it would have a low coordination ∼3; if Mo migrated subsurface into the interior of the nanoparticle it would have a high coordination ∼12. The intermediate Mo−Rh coordination number suggests that Mo is embedded in the surface of the catalyst, for instance Mo substituted into the Rh(111) surface would have a Mo−Rh CN of 9. We note that inclusion of Mo−O scattering paths yielded a poor fit, indicating no residual molybdenum oxide is present in the reduced catalyst (Table S5). To check for the presence of a pure Mo phase, we also attempted to include a Mo−Mo scattering path from a *bcc* structure, but were unable to improve the quality of the fit, indicating that no Mo clusters are formed (Table S5) within the ability to detect these via EXAFS.

3.2.3. Catalyst under Reaction Conditions. The physical and chemical states of the Rh and Mo were probed under reaction conditions in syngas at 20 bar and 250 °C using operando XAS. The Rh K-edge XANES spectra show no changes over the course of 4.5 h, demonstrating the stability of the Rh nanoparticles under reaction conditions (Figure S14). The Rh K-edge EXAFS data under steady-state reaction conditions, after 4.5 h on stream, were modeled in a similar manner to the reduced catalyst. The fitting was performed simultaneously with the reduced catalyst and the results of the fit are shown in Figures 3, S5, and Table S1. The data indicate that there is no measurable change in the local structure of the Rh nanoparticles from the reduced state during reaction. This claim is supported by ex situ XRD characterization of the catalyst measured after 36 h of syngas exposure (Figure S6). The XRD pattern shows an *fcc* Rh structure, consistent with the EXAFS, and there are no detectable Mo-containing phases. A crystallite size of ∼3.7 nm was estimated from the peak broadening, in good agreement with the nanoparticle diameter calculated from TEM imaging of the as-prepared catalyst. Similarly, high resolution TEM imaging of the $10MoO_x$/Rh catalyst after reaction showed lattice fringes consistent with *fcc* Rh, and no apparent change in the nanoparticle size (Figure S15). We note that no particular efforts were made to limit air exposure of the catalyst prior to the XRD or TEM measurements.

There are slight changes to the Mo K-edge XANES under reaction conditions that are indicative of some oxidation of the Mo (Figure S16). This change in Mo XANES, combined with the lack of change in the Rh XANES in response to a change in gas feed from pure H_2 to syngas, suggests that the Mo is primarily present at the surface of the Rh nanoparticles. This hypothesis was further supported by ex situ XPS characterization of the catalyst surface following reaction, in which the Mo is reduced below the 6+ oxidation state (Figure S4). We note that the discrepancy between oxidation states of Mo in the in situ XAS and ex situ XPS measurements is likely due to oxidation of Mo from air exposure during transfer to the XPS instrument. Upon reaching steady state under reaction conditions, the Mo EXAFS shows a strong metallic scattering path, which was again modeled by a Mo atom substituted into an *fcc* Rh lattice, as described in section 3.2.2 (Figures 4, S8, Table S2). Once again, the Mo−Rh coordination number of 8.2 ± 3.0 indicates Mo is located primarily at the catalyst surface. However, unlike the reduced catalyst, there is an additional short-range scattering feature present in the Mo EXAFS under reaction conditions. This feature was modeled by a Mo−O scattering path. The Mo−O coordination number was found to be 1.1 ± 1.2 suggesting that the average Mo atom is bound to one oxygen atom under syngas reaction conditions (x = 1 in MoO_x). The Mo−O bond length was found to be 1.93 ± 0.06 Å. For comparison, molybdenum−oxygen bond lengths are reported to be ∼1.7 Å for double bonded Mo═O and ∼1.9 Å for single bonded Mo−O.[64] The measured Mo−O bond length agrees with single bonded Mo−O, suggesting that a hydroxyl group is bound to each Mo atom at the surface of the catalyst, rather than a bare O atom.

3.3. Structure of Catalyst Surface. From the in situ XAS characterization of the catalyst, we can propose a likely structure of the Rh NP catalyst surface. Rh is present in the form of *fcc* metallic nanoparticles, with Rh metal exposed at the surface. On the basis of the coordination number of Mo−Rh bonds in the catalyst under reaction conditions, the Mo atoms are likely substituted into the Rh surface. Each Mo atom is expected to be bound to one OH group, indicated by the presence of Mo−O scattering under reaction conditions and the bond length appropriate for single bonded Mo−O. On the basis of these observations, we propose the surface structure of the catalyst consists of Mo−OH species substituted into the Rh lattice, as shown in Figure 6. This structure can be intuitively understood as resulting from a balance between two competing forces. Metallic Mo has a high surface energy,[65,66] driving Mo atoms subsurface. However, the molybdenum−oxygen bond is very strong,[67] encouraging movement of Mo to the catalyst surface where it can be oxidized. Furthermore,

DOI: 10.1021/jacs.9b07460
J. Am. Chem. Soc. 2019, 141, 19655−19668

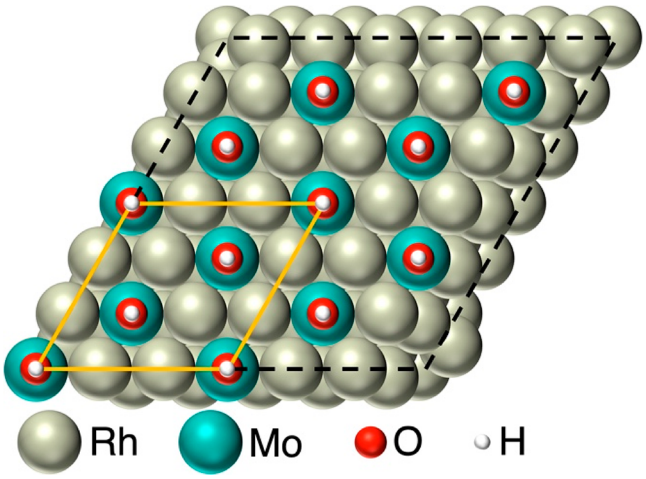

Figure 6. Proposed structure of 3MoOH/Rh(111) surface under reaction conditions. The orange parallelogram shows one unit cell, consisting of 3 Mo−OH substituted into the Rh surface.

because the Mo−O bond is much stronger than Rh−O,[67] the most favorable binding site for OH is on top of the Mo atom, rather than at the Mo−Rh interface, where the electron density would be distributed between the Mo and Rh atoms. The balance of these two forces gives rise to a structure of Mo embedded in the catalyst surface, which minimizes surface energy due to the relatively high Mo coordination, while allowing Mo to bind with OH at the surface. It is important to note that the surface structure shown in Figure 6 is highly idealized and reflects the periodicity of the unit cell used in the DFT calculations discussed subsequently. The actual MoO_x-promoted Rh catalyst surface is likely not as well-ordered as shown in Figure 6. We do not rule out the possibility that neighboring Mo−OH species may be present in the surface, but the Mo EXAFS is dominated by Mo−Rh scattering and accordingly, the Mo−Mo coordination number is expected to be very small compared to that of Mo−Rh.

To validate the proposed surface structure, DFT calculations were performed to ensure the stability of the surface and determine the bond lengths. The Mo K-edge XAS spectra that would result from this DFT-optimized structure were then simulated. The features in the Mo XANES of the $20MoO_x$/Rh catalyst under reaction conditions agree very well with those simulated from the proposed surface structure (Figure 7a). In particular there is a significant difference in the XANES spectra from 20 020 to 20 050 eV between that of Mo foil in the *bcc* structure, and Mo in the proposed *fcc* structure of Rh. This difference is clearly reproduced by the calculated XANES. Similarly, the Mo EXAFS spectrum simulated from the proposed catalyst structure also agrees well with the measured spectrum of the $20MoO_x$/Rh catalyst (Figure 7b, Table S2). This observation further supports the claim that the reduced Mo adopts the *fcc* structure of Rh under reaction conditions, rather than the *bcc* structure of pure metallic Mo.

The free energies of several potential catalyst surface structures were calculated to assess the proposed model. The energies were computed as a function of water partial pressure, in a range of values appropriate for the conversion and selectivities of the catalysts (Figure S17). The two most stable surfaces consist of Mo−O and Mo−OH species embedded in the Rh(111) facet, with one-third of the Rh sites replaced (Figure 6). The unit cell used in the computation contained 9 surface atoms, of which 3 were Mo−O or Mo−OH, so we will refer to these structures as 3MoO/Rh(111) and 3MoOH/Rh(111), respectively. We note that the thermodynamic calculations suggest that the 3MoO/Rh(111) surface structure is more stable than the proposed 3MoOH/Rh(111). However, considering that the surface of the catalyst dynamically changes under reaction conditions, it is likely that the Mo−O surface features are continually hydrogenated and dehydrogenated, leading to a mixture of Mo−O and Mo−OH surface species. In the next section, we will discuss the catalytic performance that would be expected for each of these surface structures. As an additional check of the DFT-derived catalytic structure, we calculated the expected weight percentage of Mo that would result from one-third of the Rh surface sites being replaced with Mo. Assuming 4 nm diameter spherical Rh nanoparticles with a Rh weight loading of 5%, the weight percent of Mo resulting from the 3MoOH/Rh(111) surface structure is ∼0.5%, very comparable to the experimental Mo weight loadings measured by ICP in Table 3. The thermodynamic calculations also showed that Mo−O stabilized the (211) facets relative to bare Rh, but this surface was ∼2 eV higher in energy than that of 3MoOH/Rh(111). We suggest that the high surface energy of Mo makes the Rh(211) surface a less

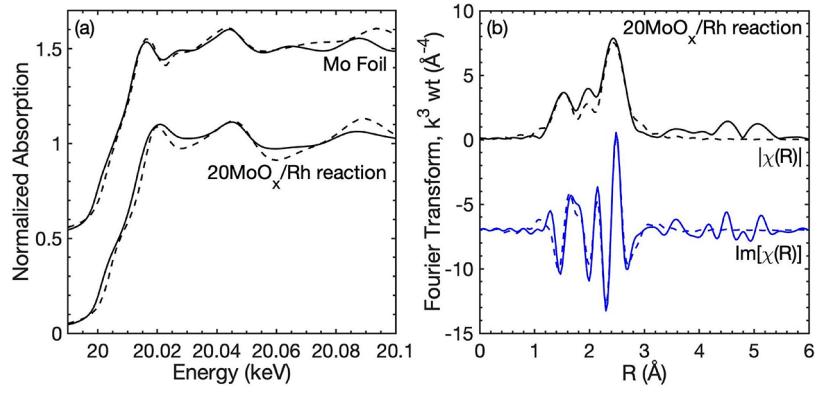

Figure 7. (a) Comparison of measured Mo K-edge XANES spectra of $20MoO_x$/Rh catalyst under reaction conditions and Mo foil to spectra simulated from 3MoOH/Rh(111) surface and *bcc* Mo metal. (b) Comparison of measured Mo K-edge EXAFS of $20MoO_x$/Rh catalyst under reaction conditions with simulated EXAFS from 3MoOH/Rh(111) surface. Measured spectra are shown as solid lines and simulated spectra are shown as dashed lines.

DOI: 10.1021/jacs.9b07460
J. Am. Chem. Soc. 2019, 141, 19655−19668

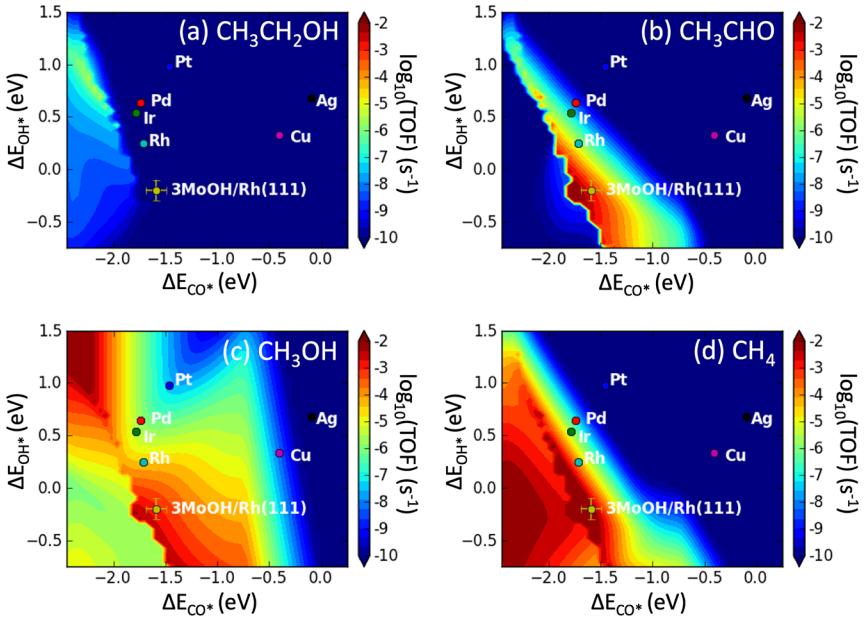

Figure 8. Rate volcano plots for (a) ethanol, (b) acetaldehyde, (c) methanol, and (d) methane production on (111) transition metal surfaces as a function of the CO binding energy (E_{CO*}) and OH binding energy (E_{OH*}) at 523 K and 20 bar. H_2:CO = 2:1, $p(CH_3OH) = p(CH_4) = p(CH_3CH_2OH) = p(CH_3CHO) = p(H_2O) = 10^{-19}$ bar. Error bars represent the uncertainty in the DFT binding energies as determined from one standard deviation of the BEEF ensemble calculation. CO and OH binding energies are formation energies of the adsorbed species with respect to CO, H_2, and H_2O gas-phase energies.

favorable binding location for Mo than the 3MoOH/Rh(111) surface.

3.4. Relationship between Surface Structure and Catalytic Properties. Having assessed the performance of the MoO_3-promoted Rh catalysts in syngas conversion reactions and identified the structure of the catalyst surface, we now examine how the structure and chemistry of the surface give rise to its catalytic properties. DFT calculations on the Rh(111) and 3MoOH/Rh(111) catalyst surfaces show that the presence of Mo−OH does not significantly affect the CO binding site or binding energy (Table S6). In particular, linear CO adsorption to a single Rh atom is the most stable on both surfaces (Figure S18) and CO binding to the Mo atom or at the Rh/Mo interface is less energetically favorable. This conclusion is supported experimentally by DRIFTS studies of CO bound to the catalyst surface, which show the strongest intensity for linearly bound CO, no additional CO binding configurations with MoO_3 present, and no significant difference in CO vibration frequency between the catalysts with and without MoO_3 promotion (Figure S19). In contrast, DFT calculations show that OH binding is stabilized on the MoO_3-promoted Rh surface (Table S6) due to the creation of an energetically favorable binding site on the Mo (Figure S18). The OH stabilization can equivalently be thought of as a stabilization of O binding to the surface, due to existing scaling relations between the OH and O binding energies.[68] The stabilization of oxygen binding on the promoted catalyst surface has two effects. First, it decreases the difference between the energy of *C + *O and *CO by lowering the energy of the dissociated state. This, in turn, lowers the barrier for CO dissociation, due to scaling relations between the transition state energy and the energy difference between the dissociated and associated forms of CO.[69] As a result of the lower barrier for CO dissociation, hydrocarbon production is activated on the 3MoOH/Rh(111) surface, a reaction pathway that is disfavored on the pure Rh(111) surface.[7] Following CO dissociation, there will be two OH groups bound to the Mo site, as shown in Figure S18. This configuration is higher in energy than the 3MoOH/Rh(111) surface (Figure S17), so it is expected that one of the OH groups will be quickly hydrogenated to form water and restore the 1:1 Mo:O ratio that is observed under steady-state reaction conditions. Second, the strong O binding site creates a pathway for methanol formation in the sequence *CHO, *CH_2O, *OCH_3, CH_3OH, which is disfavored on the unpromoted Rh(111) surface.[53] In this pathway, *CH_2O lies flat on the surface and *OCH_3 binds to the surface through the oxygen atom,[70] configurations which are enabled by the more favorable interaction between O and the MoO_3-promoted catalyst surface. These effects are readily seen in the enhanced activity of the catalyst, and the product distribution, which favors methane and methanol.

Because the thermodynamic calculations predict that the 3MoO/Rh(111) surface is more stable than the proposed 3MoOH/Rh(111) surface, the CO and OH adsorption energies on the 3MoO/Rh(111) surface were also calculated (Table S6). Unsurprisingly, the two surfaces have identical CO adsorption energies, since the most stable CO binding site is on the Rh atom in both cases. The OH adsorption energies are also nearly the same, with values of −0.20 eV and −0.23 eV for the 3MoOH/Rh(111) and 3MoO/Rh(111) surfaces, respectively. The similarity between these adsorption energies implies that the catalytic properties of the two surfaces are nearly identical. In fact, because a typical CO hydrogenation reaction pathway involves multiple hydrogen adsorption and reaction steps, it is expected that the Mo−OH surface species will undergo multiple dehydrogenation and hydrogenation reactions. Therefore, Mo−OH and Mo−O would both be expected intermediates in a typical catalytic cycle, and it is not surprising that both surface structures yield nearly identical catalytic reactivity.

DOI: 10.1021/jacs.9b07460
J. Am. Chem. Soc. 2019, 141, 19655−19668

The adsorption energies of reaction intermediates on the 3MoOH/Rh(111) surface were calculated in order to determine the rates of formation of different products over the MoO_3-promoted Rh catalyst. Transition state energies were computed for CH−OH dissociation and HCO−H bond formation, which are considered to be rate-limiting steps for methane and methanol synthesis, respectively. We find that these energies can be expressed as linear combinations of the CO and OH binding energies, following the same scaling relations for several unpromoted metal surfaces (Figure S20). On the basis of these scaling relations, a microkinetic model of the CO hydrogenation reactions can be built using CO and OH binding energies as descriptors, as has been reported previously.[53] Because the pure Rh and MoO_3-promoted Rh catalysts follow the same scaling relations, the product formation rates over the two catalyst surfaces can be directly compared on two-dimensional rate volcano plots (Figure 8). On the 3MoOH/Rh(111) surface, the turnover frequencies for methane and methanol are predicted to increase by ∼2 orders of magnitude relative to the unpromoted Rh(111) surface. For comparison, experimental measurements showed up to 55- and >62-fold increases in methane and methanol TOFs, respectively, on the MoO_3-promoted Rh catalysts, in good agreement with the rate increase predicted from DFT.

Although there is excellent agreement between theory and experiment for the methane and methanol TOFs, there is one significant discrepancy between the experimental and calculated product distributions: the calculations predict a significantly higher acetaldehyde TOF in the MoO_3-promoted catalysts and no significant change in ethanol TOF. Instead, the experiments show an increase in ethanol formation and no acetaldehyde production (Table S3). We therefore propose that MoO_3 has an additional promotional role, beyond stabilizing OH binding. Because the product distribution shows an increase in the hydrogenation rate of reaction intermediates in the MoO_3-promoted catalysts, we suggest that the hydrogen in Mo−OH participates in hydrogenation steps of the reaction sequence. On an unpromoted Rh(111) surface the adsorption energy of hydrogen is −0.28 eV, much higher than the CO adsorption energy of −1.71 eV (Table S6). As a result, the unpromoted Rh(111) surface is expected to have a very high ratio of CO:H coverage. On the 3MoOH/Rh(111) surface, hydrogen atoms on Mo−OH are located in close proximity to reactive sites on Rh. We propose that the hydrogen in Mo−OH can spillover to adsorbed reaction intermediates on the Rh surface, leading to rapid hydrogenation rates and leaving behind Mo−O. DFT calculations were performed to determine the hydrogen adsorption energy on the Mo−O sites that would remain following hydrogen spillover. The most stable adsorption site for hydrogen was found to be on top of the O atom, and have an energy of −0.27 eV (Table S6). Although this hydrogen adsorption energy is similar to that of unpromoted Rh (111), the binding site on Mo−O is not available for CO adsorption. As a result, the 3MoOH/Rh(111) catalyst surface has certain sites which are reserved for H adsorption, thereby increasing the surface coverage of hydrogen and in turn, hydrogenation rates.

Although hydrogen spillover from Mo to Rh has not been directly observed, there is evidence for the reverse process, H spillover from Rh to MoO_3 during catalyst reduction. The movement of hydrogen between Rh and MoO_x is clearly evident by comparing the TPR profiles of the Rh, MoO_3, and $10MoO_x$/Rh catalysts (Figure S11). The $10MoO_x$/Rh catalyst shows a MoO_x reduction feature in the temperature range of 200−250 °C, whereas the MoO_3 catalyst shows no reduction at temperatures below 400 °C. This suggests that reduction of MoO_3 at temperatures below 250 °C is enabled by hydrogen spillover from Rh. This result is further demonstrated by in situ XAS experiments (Figure 9), based on the following analysis.

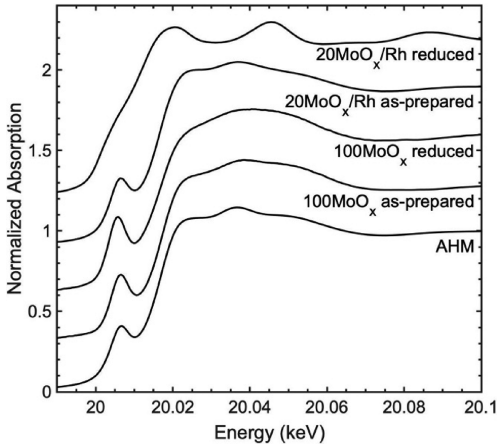

Figure 9. In situ Mo K-edge XANES in ALD MoO_3 samples with and without Rh present. Samples are shown in the as-prepared state (20 sccm He, 1 atm, 25 °C) and the reduced state (20 sccm H_2, 1 atm, 250 °C). AHM refers to ammonium heptamolybdate tetrahydrate. Spectra are offset for clarity.

The Mo K-edge XANES spectra for catalysts with and without Rh are very similar in the as-prepared state, and exhibit similarities to that of AHM, as discussed above. After heating the catalyst to 250 °C in H_2, the Mo in the $20MoO_x$/Rh catalyst is reduced (x = 3 to x = 0). In contrast, the Mo XANES for the $100MoO_x$ catalyst, which contains no Rh, shows behavior consistent with desorption of water from the surface, but the Mo oxidation state remains relatively unchanged (Figure S21; x = 3). We therefore conclude that hydrogen spillover from Rh onto MoO_3 enables the reduction of MoO_3 in the catalyst containing Rh. Due to the presence of hydrogen on Mo−OH, we suggest that hydrogen may spillover in the reverse direction, from Mo−OH to Rh, during reaction. Given the structure of the MoO_3-promoted Rh surface, the hydrogen on Mo−OH sites are in close proximity to adsorbed reaction intermediates on the Rh surface. The Mo−O can then be readily rehydrogenated from the gas phase because hydrogen does not compete with CO for the Mo−O binding site. The ready availability of reactive hydrogen enables fast hydrogenation, leading to improved catalytic activity and fully hydrogenated products. In support of this proposed mechanism, there are several reports in the literature showing hydrogen spillover onto molybdenum oxide,[71,72] and there are many applications of metal oxides acting as hydrogen sources via spillover.[73,74]

4. CONCLUSIONS

We have used atomic layer deposition to promote Rh nanoparticles with ultrathin layers of MoO_3, which has enabled a fundamental study of the role of MoO_3 in promoting the performance of these catalysts. The results show that MoO_3 deposits preferentially on the Rh_2O_3 nanoparticles rather than the SiO_2 support. Through catalytic testing in syngas, we find that MoO_3 increases the catalytic activity of Rh and shifts

DOI: 10.1021/jacs.9b07460
J. Am. Chem. Soc. 2019, 141, 19655−19668

product selectivity toward methanol, methane, and fully hydrogenated products. The activity increases despite a significant decrease in the number of CO adsorption sites, leading to a 66-fold enhancement in TOF. Structural characterization of the catalyst surface by in situ XAS and predictive DFT calculations showed that Mo−OH species are substituted into the Rh(111) surface under reaction conditions. Calculations show that the presence of Mo−OH in the Rh(111) surface helps stabilize oxygen-containing intermediates, thus leading to a greater rate of CO dissociation and opening a new pathway for methanol formation that is not present in the unpromoted catalyst. Finally, we suggest that hydrogen spillover from Mo−OH may enhance the hydrogenation rate of nearby reaction intermediates on the Rh surface. On the basis of the insights gained from this study, we suggest that molybdenum oxide may be an effective promoter in a variety of other catalytic processes, namely, hydrogenation reactions based on the observation of fully hydrogenated products over the MoO_x-promoted Rh catalysts, and oxidation reactions where the inclusion of Mo can be used to tune the oxygen adsorption energy. Furthermore, the strategy used in this study of combining precise synthesis by ALD, in situ characterization, and DFT calculations can be applied to a variety of catalyst systems to uncover structure−property relationships.

■ ASSOCIATED CONTENT

Supporting Information

The Supporting Information is available free of charge at https://pubs.acs.org/doi/10.1021/jacs.9b07460.

Spectroscopic characterization including XPS, DRIFTS, and details of in situ EXAFS fits; X-ray diffraction measurements; Growth curve of MoO_3 ALD; Thermodynamic calculations of surface stability; DFT calculations of adsorbate binding energies (PDF)

Crystal data for 3MoOH/Rh(111) (CIF)

Crystal data for 3MoO/Rh(111) (CIF)

■ AUTHOR INFORMATION

Corresponding Author

*sbent@stanford.edu

ORCID

Arun S. Asundi: 0000-0003-0333-6784
Adam S. Hoffman: 0000-0002-7682-4108
Fernando D. Vila: 0000-0002-6508-4896
Nuoya Yang: 0000-0002-4625-9806
Joseph A. Singh: 0000-0001-5249-2121
Li Zeng: 0000-0001-6390-0370
James A. Raiford: 0000-0003-2126-5422
Frank Abild-Pedersen: 0000-0002-1911-074X
Simon R. Bare: 0000-0002-4932-0342
Stacey F. Bent: 0000-0002-1084-5336

Present Address

[▽]Karlsruhe Institute of Technology, 76131 Karlsruhe, Germany.

Notes

The authors declare no competing financial interest.

■ ACKNOWLEDGMENTS

We gratefully acknowledge the support from the Global Climate and Energy Project (GCEP) at Stanford and the U.S. Department of Energy, Office of Science, Office of Basic Energy Sciences, Chemical Sciences, Geosciences, and Biosciences Division, Catalysis Science Program to the SUNCAT Center for Interface Science and Catalysis. Use of the Stanford Synchrotron Radiation Lightsource, SLAC National Accelerator Laboratory is supported by the U.S. Department of Energy, Office of Basic Energy Sciences under Contract No. DE-AC02-76SF00515. Co-ACCESS is supported by the U.S. Department of Energy, Office of Science, Office of Basic Energy Sciences, Chemical Sciences, Geosciences and Biosciences. Part of this work was performed at the Stanford Nano Shared Facilities (SNSF), supported by the National Science Foundation under award ECCS-1542152. The FEFF XANES simulations used resources of the National Energy Research Scientific Computing Center (NERSC), a U.S. Department of Energy Office of Science User Facility operated under Contract No. DE-AC02-05CH11231. We thank Verena Streibel for generating the volcano plots based on the DFT calculations.

■ REFERENCES

(1) Subramani, V.; Gangwal, S. K. A Review of Recent Literature to Search for an Efficient Catalytic Process for the Conversion of Syngas to Ethanol. *Energy Fuels* **2008**, *22* (2), 814−839.

(2) Luk, H. T.; Mondelli, C.; Ferré, D. C.; Stewart, J. A.; Pérez-Ramírez, J. Status and Prospects in Higher Alcohols Synthesis from Syngas. *Chem. Soc. Rev.* **2017**, *46* (5), 1358−1426.

(3) Ao, M.; Pham, G. H.; Sunarso, J.; Tade, M. O.; Liu, S. Active Centers of Catalysts for Higher Alcohol Synthesis from Syngas: A Review. *ACS Catal.* **2018**, *8*, 7025−7050.

(4) Spivey, J. J.; Egbebi, A. Heterogeneous Catalytic Synthesis of Ethanol from Biomass-Derived Syngas. *Chem. Soc. Rev.* **2007**, *36*, 1514−1528.

(5) Gerber, M. A.; Gray, M. J.; Stevens, D. J.; White, J. F.; Thompson, B. L. *Optimization of Rhodium-Based Catalysts for Mixed Alcohol Synthesis—2009 Progress Report*; U.S. Department of Energy, 2010.

(6) Albrecht, K. O.; Glezakou, V.-A.; Rousseau, R.; Engelhard, M. H.; Varga, T.; Li, X.; Mei, D.; Windisch, C. F.; Kathmann, S. M.; Lemmon, T.; Gray, M. J.; Hart, T. R.; Thompson, B. L.; Gerber, M. A. *Rh-Based Mixed Alcohol Synthesis Catalysts: Characterization and Computational Report*; U.S. Department of Energy, 2013.

(7) Yang, N.; Medford, A. J.; Liu, X.; Studt, F.; Bligaard, T.; Bent, S. F.; Norskov, J. K. Intrinsic Selectivity and Structure Sensitivity of Rhodium Catalysts for C_{2+} Oxygenate Production. *J. Am. Chem. Soc.* **2016**, *138*, 3705−3714.

(8) Choi, Y.; Liu, P. Mechanism of Ethanol Synthesis from Syngas on Rh(111). *J. Am. Chem. Soc.* **2009**, *131* (36), 13054−13061.

(9) Kapur, N.; Hyun, J.; Shan, B.; Nicholas, J. B.; Cho, K. Ab Initio Study of CO Hydrogenation to Oxygenates on Reduced Rh Terraces and Stepped Surfaces. *J. Phys. Chem. C* **2010**, *114*, 10171−10182.

(10) Bhasin, M. M.; Bartley, W. J.; Ellgen, P. C.; Wilson, T. P. Synthesis Gas Conversion over Supported Rhodium and Rhodium-Iron Catalysts. *J. Catal.* **1978**, *54*, 120−128.

(11) Filot, I. A. W.; Broos, R. J. P.; van Rijn, J. P. M.; van Heugten, G. J. H. A.; van Santen, R. A.; Hensen, E. J. M. First-Principles-Based Microkinetics Simulations of Synthesis Gas Conversion on a Stepped Rhodium Surface. *ACS Catal.* **2015**, *5*, 5453−5467.

(12) Sachtler, W. M. H.; Ichikawa, M. Catalytic Site Requirements for Elementary Steps in Syngas Conversion to Oxygenates Over Promoted Rhodium. *J. Phys. Chem.* **1986**, *90* (20), 4752−4758.

(13) Zhang, R.; Duan, T.; Wang, B.; Ling, L. Unraveling the Role of Support Hydroxyls and Its Effect on the Selectivity of C_2 Species over

DOI: 10.1021/jacs.9b07460
J. Am. Chem. Soc. 2019, 141, 19655−19668

Rh/Gamma-Al_2O_3 Catalyst in Syngas Conversion: A Theoretical Study. *Appl. Surf. Sci.* **2016**, *379*, 384−394.
(14) Mawson, S.; McCutchen, M. S.; Lim, P. K.; Roberts, G. W. Thermodynamics of Higher Alcohols Synthesis. *Energy Fuels* **1993**, *7* (2), 257−267.
(15) Spath, P. L.; Dayton, D. C. *Preliminary Screening—Technical and Economic Assessment of Synthesis Gas to Fuels and Chemicals with Emphasis on the Potential for Biomass-Derived Syngas*; U.S. Department of Energy, 2003.
(16) Xiaoding, X. U.; Doesburg, E. B. M.; Scholten, J. J. F. Synthesis of Higher Alcohols from Syngas - Recently Patented Catalysts and Tentative Ideas on the Mechanism. *Catal. Today* **1987**, *2*, 125−170.
(17) Medford, A. J.; Lausche, A. C.; Abild-Pedersen, F.; Temel, B.; Schjødt, N. C.; Nørskov, J. K.; Studt, F. Activity and Selectivity Trends in Synthesis Gas Conversion to Higher Alcohols. *Top. Catal.* **2014**, *57*, 135−142.
(18) Wang, J.; Liu, Z.; Zhang, R.; Wang, B. Ethanol Synthesis from Syngas on the Stepped Rh(211) Surface: Effect of Surface Structure and Composition. *J. Phys. Chem. C* **2014**, *118*, 22691−22701.
(19) Gerber, M. A.; White, J. F.; Gray, M.; Stevens, D. J. *Evaluation of Promoters for Rhodium-Based Catalysts for Mixed Alcohol Synthesis*; U.S. Department of Energy, 2008.
(20) *Progress in C1 Chemistry in Japan*; Elsevier, 1989.
(21) Mei, D.; Rousseau, R.; Kathmann, S. M.; Glezakou, V.; Engelhard, M. H.; Jiang, W.; Wang, C.; Gerber, M. A.; White, J. F.; Stevens, D. J. Ethanol Synthesis from Syngas over Rh-Based/SiO_2 Catalysts: A Combined Experimental and Theoretical Modeling Study. *J. Catal.* **2010**, *271*, 325−342.
(22) Yang, N.; Liu, X.; Asundi, A. S.; Nørskov, J. K.; Bent, S. F. The Role of Sodium in Tuning Product Distribution in Syngas Conversion by Rh Catalysts. *Catal. Lett.* **2018**, *148*, 289−297.
(23) Carrillo, P.; Shi, R.; Teeluck, K.; Senanayake, S. D.; White, M. G. *In Situ* Formation of FeRh Nanoalloys for Oxygenate Synthesis. *ACS Catal.* **2018**, *8*, 7279−7286.
(24) Liu, Y.; Göeltl, F.; Ro, I.; Ball, M. R.; Sener, C.; Aragão, I. B.; Zanchet, D.; Huber, G. W.; Mavrikakis, M.; Dumesic, J. A. Synthesis Gas Conversion over Rh-Based Catalysts Promoted by Fe and Mn. *ACS Catal.* **2017**, *7*, 4550−4563.
(25) Mao, W.; Su, J.; Zhang, Z.; Xu, X.; Fu, D.; Dai, W.; Xu, J.; Zhou, X.; Han, Y. A Mechanistic Basis for the Effects of Mn Loading on C_{2+} Oxygenates Synthesis Directly from Syngas over Rh-MnO_x/SiO_2 Catalysts. *Chem. Eng. Sci.* **2015**, *135*, 301−311.
(26) Matsubu, J. C.; Zhang, S.; DeRita, L.; Marinkovic, N. S.; Chen, J. G.; Graham, G. W.; Pan, X.; Christopher, P. Adsorbate-mediated Strong Metal-support Interactions in Oxide-supported Rh Catalysts. *Nat. Chem.* **2017**, *9*, 120−127.
(27) Liu, Y.; Murata, K.; Inaba, M.; Takahara, I.; Okabe, K. Synthesis of Ethanol from Syngas over Rh/$Ce_{1-x}Zr_xO_2$ Catalysts. *Catal. Today* **2011**, *164*, 308−314.
(28) Kip, B. J.; Hermans, E. G. F.; van Wolput, J. H. M. C.; Hermans, N. M. A.; van Grondelle, J.; Prins, R. Hydrogenation of Carbon Monoxide over Rhodium/Silica Catalysts Promoted with Molybdenum Oxide and Thorium Oxide. *Appl. Catal.* **1987**, *35*, 109−139.
(29) Szenti, I.; Bugyi, L.; Kónya, Z. The Promotion of CO Dissociation by Molybdenum Oxide Overlayers on Rhodium. *Surf. Sci.* **2017**, *657*, 1−9.
(30) van den Berg, F. G. A.; Glezer, J. H. E.; Sachtler, W. M. H. The Role of Promoters in CO/H_2 Reactions: Effects of MnO and MoO_2 in Silica-Supported Rhodium Catalysts. *J. Catal.* **1985**, *93*, 340−352.
(31) Mao, W.; Su, J.; Zhang, Z.; Xu, X.; Dai, W.; Fu, D.; Xu, J.; Zhou, X.; Han, Y. Kinetics Study of C_{2+} Oxygenates Synthesis from Syngas over Rh−MnO_x/SiO_2 Catalysts. *Chem. Eng. Sci.* **2015**, *135*, 312−322.
(32) Hu, J.; Wang, Y.; Cao, C.; Elliott, D. C.; Stevens, D. J.; White, J. F. Conversion of Biomass-Derived Syngas to Alcohols and C_2 Oxygenates Using Supported Rh Catalysts in a Microchannel Reactor. *Catal. Today* **2007**, *120*, 90−95.
(33) Liu, J.; Tao, R.; Guo, Z.; Regalbuto, J. R.; Marshall, C. L.; Klie, R. F.; Miller, J. T.; Meyer, R. J. Selective Adsorption of Manganese onto Rhodium for Optimized Mn/Rh/SiO_2 Alcohol Synthesis Catalysts. *ChemCatChem* **2013**, *5*, 3665−3672.
(34) Zhang, L.; Ball, M. R.; Liu, Y.; Kuech, T. F.; Huber, G. W.; Mavrikakis, M.; Hermans, I.; Dumesic, J. A. Synthesis Gas Conversion over Rh/Mo Catalysts Prepared by Atomic Layer Deposition. *ACS Catal.* **2019**, *9*, 1810−1819.
(35) Singh, J. A.; Yang, N.; Bent, S. F. Nanoengineering Heterogeneous Catalysts by Atomic Layer Deposition. *Annu. Rev. Chem. Biomol. Eng.* **2017**, *8*, 1−22.
(36) O'Neill, B. J.; Jackson, D. H. K.; Lee, J.; Canlas, C.; Stair, P. C.; Marshall, C. L.; Elam, J. W.; Kuech, T. F.; Dumesic, J. A.; Huber, G. W. Catalyst Design with Atomic Layer Deposition. *ACS Catal.* **2015**, *5*, 1804−1825.
(37) Lu, J.; Elam, J. W.; Stair, P. C. Atomic Layer Deposition - Sequential Self-Limiting Surface Reactions for Advanced Catalyst "Bottom-up" Synthesis. *Surf. Sci. Rep.* **2016**, *71* (2), 410−472.
(38) Cao, K.; Cai, J.; Liu, X.; Chen, R. Review Article: Catalysts Design and Synthesis via Selective Atomic Layer Deposition. *J. Vac. Sci. Technol., A* **2018**, *36*, 1−12.
(39) Stair, P. C. Advanced Synthesis for Advancing Heterogeneous Catalysis. *J. Chem. Phys.* **2008**, *128*, 1−4.
(40) Zhang, B.; Qin, Y. Interface Tailoring of Heterogeneous Catalysts by Atomic Layer Deposition. *ACS Catal.* **2018**, *8*, 10064−10081.
(41) Nonneman, L. E. Y.; Bastein, A. G. T. M.; Ponec, V.; Burch, R. Role of Impurities in the Enhancement of C_2-Oxygenates Activity: Supported Rhodium Catalysts. *Appl. Catal.* **1990**, *62*, 23−28.
(42) Libera, J. A.; Elam, J. W.; Pellin, M. J. Conformal ZnO Coatings on High Surface Area Silica Gel Using Atomic Layer Deposition. *Thin Solid Films* **2008**, *516* (18), 6158−6166.
(43) Hoffman, A. S.; Singh, J. A.; Bent, F.; Bare, S. R. In Situ Observation of Phase Changes of a Silica-Supported Cobalt Catalyst for the Fischer−Tropsch Process by the Development of a Synchrotron-Compatible In Situ/Operando Powder X-Ray Diffraction Cell. *J. Synchrotron Radiat.* **2018**, *25*, 1673−1682.
(44) Ravel, B.; Newville, M. ATHENA, ARTEMIS, HEPHAESTUS: Data Analysis for X-Ray Absorption Spectroscopy Using IFEFFIT. *J. Synchrotron Radiat.* **2005**, *12*, 537−541.
(45) Bunker, G. *Introduction to XAFS: A Practical Guide to X-Ray Absorption Fine Structure Spectroscopy*; Cambridge University Press, 2010.
(46) Rehr, J. J.; Kas, J. J.; Prange, M. P.; Sorini, A. P.; Takimoto, Y.; Vila, F. *Ab initio* Theory and Calculations of X-ray Spectra. *C. R. Phys.* **2009**, *10*, 548−559.
(47) Rehr, J. J.; Kas, J. J.; Vila, F. D.; Prange, M. P.; Jorissen, K. Parameter-free Calculations of X-ray Spectra with FEFF9. *Phys. Chem. Chem. Phys.* **2010**, *12*, 5503−5513.
(48) Giannozzi, P.; Baroni, S.; Bonini, N.; Calandra, M.; Car, R.; Cavazzoni, C.; Ceresoli, D.; Chiarotti, G. L.; Cococcioni, M.; Dabo, I.; Corso, A. D.; de Gironcoli, S.; Fabris, S.; Fratsei, G.; Gebauer, R.; Gerstmann, U.; Gougoussis, C.; Kokalj, A.; Lazzeri, M.; Martin-Samos, L.; Marzari, N.; Mauri, F.; Mazzarello, R.; Paolini, S.; Pasquarello, A.; Paulatto, L.; Sbraccia, C.; Scandolo, S.; Sclauzero, G.; Setsonen, A. P.; Smogunov, A.; Umari, P.; Wentzcovitch, R. M. QUANTUM ESPRESSO: A Modular and Open-Source Software Project for Quantum Simulations of Materials. *J. Phys.: Condens. Matter* **2009**, *21*, 1−19.
(49) Bahn, S. R.; Jacobsen, K. W. An Object-Oriented Scripting Interface to a Legacy Electronic Structure Code. *Comput. Sci. Eng.* **2002**, *4* (3), 56−66.
(50) Wellendorff, J.; Lundgaard, K. T.; Møgelhøj, A.; Petzold, V.; Landis, D. D.; Nørskov, J. K.; Bligaard, T.; Jacobsen, K. W. Density Functionals for Surface Science: Exchange-Correlation Model Development with Bayesian Error Estimation. *Phys. Rev. B: Condens. Matter Mater. Phys.* **2012**, *85*, 1−23.
(51) Monkhorst, H. J.; Pack, J. D. Special Points for Brillouin-Zone Integration. *Phys. Rev. B* **1976**, *13* (12), 5188−5192.

DOI: 10.1021/jacs.9b07460
J. Am. Chem. Soc. 2019, 141, 19655−19668

(52) Medford, A. J.; Shi, C.; Hoffmann, M. J.; Lausche, A. C.; Fitzgibbon, S. R.; Bligaard, T.; Nørskov, J. K. CatMAP: A Software Package for Descriptor-Based Microkinetic Mapping of Catalytic Trends. *Catal. Lett.* **2015**, *145*, 794−807.
(53) Schumann, J.; Medford, A. J.; Yoo, J. S.; Zhao, Z.; Bothra, P.; Cao, A.; Studt, F.; Abild-Pedersen, F.; Nørskov, J. K. Selectivity of Synthesis Gas Conversion to C_{2+} Oxygenates on fcc(111) Transition-Metal Surfaces. *ACS Catal.* **2018**, *8*, 3447−3453.
(54) Yang, N.; Yoo, J. S.; Schumann, J.; Bothra, P.; Singh, J. A.; Valle, E.; Abild-Pedersen, F.; Nørskov, J. K.; Bent, S. F. Rh-MnO Interface Sites Formed by Atomic Layer Deposition Promote Syngas Conversion to Higher Oxygenates. *ACS Catal.* **2017**, *7*, 5746−5757.
(55) Van't Blik, H. F. J.; Van Zon, J. B. A. D.; Huizinga, T.; Vis, J. C.; Koningsberger, D. C.; Prins, R. Structure of Rhodium in an Ultradispersed Rh/Al_2O_3 Catalyst as Studied by EXAFS and Other Techniques. *J. Am. Chem. Soc.* **1985**, *107* (11), 3139−3147.
(56) Cramer, S. P.; Eccles, T. K.; Kutzler, F. W.; Hodgson, K. O.; Mortenson, L. E. Molybdenum X-Ray Absorption Edge Spectra. The Chemical State of Molybdenum in Nitrogenase. *J. Am. Chem. Soc.* **1976**, *98* (5), 1287−1288.
(57) Rentería, M.; Traverse, A.; Anunziata, O. A.; Lede, E. J.; Pierella, L.; Requejo, F. G. In Situ and Ex Situ XANES Study of Nanodispersed Mo Species in Zeolites Used in Fine Chemistry Catalysis. *J. Synchrotron Radiat.* **2001**, *8*, 631−633.
(58) Diskus, M.; Nilsen, O.; Fjellvåg, H. Growth of Thin Films of Molybdenum Oxide by Atomic Layer Deposition. *J. Mater. Chem.* **2011**, *21*, 705−710.
(59) Nandi, D. K.; Sarkar, S. K. Atomic Layer Deposition of Molybdenum Oxide for Solar Cell Application. *Appl. Mech. Mater.* **2014**, *492*, 375−379.
(60) Vis, J.C.; Van't Buk, H. F.J.; Huizinga, T.; Van Grondelle, J.; Prins, R. Reduction and Oxidation of Rh/Al_2O_3 and Rh/TiO_2 Catalysts as Studied by Temperature-Programmed Reduction and Oxidation. *J. Mol. Catal.* **1984**, *25*, 367−378.
(61) Marinkovic, N. S.; Sasaki, K.; Adzic, R. R. Nanoparticle Size Evaluation of Catalysts by EXAFS: Advantages and Limitations. *Zast. Mater.* **2016**, *57*, 101−109.
(62) Arnoldy, P.; De Jonge, J. C. M.; Moulijn, J. A. Temperature-Programed Reduction of Molybdenum(VI) Oxide and Molybdenum-(IV) Oxide. *J. Phys. Chem.* **1985**, *89* (21), 4517−4526.
(63) Chary, K. V. R.; Bhaskar, T.; Kishan, G.; Reddy, K. R. Characterization and Reactivity of Molybdenum Oxide Catalysts Supported on Niobia. *J. Phys. Chem. B* **2001**, *105*, 4392−4399.
(64) Rao, M. C.; Ravindranadh, K.; Katsuri, A.; Shekhawat, M. S. Structural Stoichiometry and Phase Transitions of MoO_3 Thin Films for Solid State Microbatteries. *Res. J. Recent Sci.* **2013**, *2* (4), 67−73.
(65) Tyson, W. R.; Miller, W. A. Surface Free Energies of Solid Metals: Estimation From Liquid Surface Tension Measurements. *Surf. Sci.* **1977**, *62*, 267−276.
(66) Tran, R.; Xu, Z.; Radhakrishnan, B.; Winston, D.; Sun, W.; Persson, K. A.; Ong, S. P. Data Descriptor: Surface Energies of Elemental Crystals. *Sci. Data* **2016**, *3*, 1−13.
(67) Dean, J. A. *Lange's Handbook of Chemistry*; Norbert Adolph Lange, 1999.
(68) Fernández, E. M.; Moses, P. G.; Toftelund, A.; Hansen, H. A.; Martínez, J. I.; Abild-Pedersen, F.; Kleis, J.; Hinnemann, B.; Rossmeisl, J.; Bligaard, T.; Nørskov, J. K. Scaling Relationships for Adsorption Energies on Transition Metal Oxide, Sulfide, and Nitride Surfaces. *Angew. Chem., Int. Ed.* **2008**, *47* (25), 4683−4686.
(69) Wang, S.; Temel, B.; Shen, J.; Jones, G.; Grabow, L. C.; Studt, F.; Bligaard, T.; Abild-Pedersen, F.; Christensen, C. H.; Nørskov, J. K. Universal Brønsted-Evans-Polanyi Relations for C−C, C−O, C−N, N−O, N−N, and O−O Dissociation Reactions. *Catal. Lett.* **2011**, *141* (3), 370−373.
(70) Studt, F.; Abild-Pedersen, F.; Wu, Q.; Jensen, A. D.; Temel, B.; Grunwaldt, J. D.; Norskov, J. K. CO Hydrogenation to Methanol on Cu-Ni Catalysts: Theory and Experiment. *J. Catal.* **2012**, *293*, 51−60.
(71) Chen, L.; Cooper, A. C.; Pez, G. P.; Cheng, H. On the Mechanisms of Hydrogen Spillover in MoO_3. *J. Phys. Chem. C* **2008**, *112* (6), 1755−1758.
(72) Sermon, P. A.; Bond, G. C. Studies of Hydrogen Spillover. *J. Chem. Soc., Faraday Trans. 1* **1976**, *72*, 730−744.
(73) Prins, R. Hydrogen Spillover. Facts and Fiction. *Chem. Rev.* **2012**, *112*, 2714−2738.
(74) Conner, W. C.; Falconer, J. L. Spillover in Heterogeneous Catalysis. *Chem. Rev.* **1995**, *95* (3), 759−788.

DOI: 10.1021/jacs.9b07460
J. Am. Chem. Soc. 2019, 141, 19655−19668